ARTICLES
https://doi.org/10.1038/s41561-021-00860-8
nature geoscience

Great Plains storm intensity since the last glacial controlled by spring surface warming

Chijun Sun[1]✉, Timothy M. Shanahan[1], Pedro N. DiNezio[2,3], Nicholas P. McKay[4] and Priyadarsi D. Roy[5]

Mesoscale convective systems (MCSs) supply a substantial portion of warm-season rainfall to the Great Plains of North America, and they are responsible for severe weather and flooding across the central United States. However, little is known about past behaviour and long-term drivers of these systems, limiting our ability to predict future extreme weather patterns in this region. Here, we generate a 20,000-year-long multiproxy record of storm intensity and hydroclimate variability from central Texas in the southern Great Plains and use transient climate model simulations to diagnose the dynamics of reconstructed changes in the climate of this region. We find that southern Great Plains storm intensity responded dynamically to external forcings associated with glacial boundary conditions and orbital forcing via changes in seasonal land surface warming. Springtime land surface warming steepens the zonal pressure gradient, producing an intensified southerly Great Plains low-level jet, enhancing southerly moisture transport and increasing springtime MCS intensity. Climate models predict a strengthening of the low-level jet in response to future warming, which our study suggests will lead to enhanced MCS activity and an increase in extreme weather across the Great Plains.

Much of the rainfall over the central United States is generated by mesoscale convective systems (MCSs), large (>100 km) organized convective storms[1] that produce intense precipitation and are often accompanied by flooding, hail and damaging winds. Economic losses due to convective storms in the United States exceed US$10 billion annually[2], the majority of which is associated with MCSs[3]. Over the past few decades, the frequency and intensity of central-US MCSs has increased dramatically[4], far beyond the predicted rate of increase in precipitable water (~7% per °C warming) based on the thermodynamic Clausius–Clapeyron relationship. This trend has been attributed to a strengthening southerly low-level flow and the associated Great Plains low-level jet (LLJ), which provides the moisture and energy required for MCS development[4]. Simulations of future warming with global general circulation models (GCMs) predict a strengthening of the LLJ in response to continued surface warming of the eastern Rockies and western Great Plains, but there is little consensus about the changes in MCS development and overall precipitation, which is partly due to the relatively coarse atmospheric resolution adopted in these GCMs[5–10].

Past changes in Great Plains MCS activity

To improve our understanding of the sensitivity of central-US hydroclimate and extreme rainfall to climate change, we generate a multiproxy reconstruction of changes in MCS activity and vegetation in the southern Great Plains from the sediments of Hall's Cave, Texas (30° 8′ 11″ N, 99° 32′ 6″ W). This region is among the most poorly studied in North America, with few continuous, well-dated and high-resolution palaeoclimate records. Hall's Cave is an exception: 37 radiocarbon dates provide a robust, linear age–depth model spanning the past 20,000 years (Extended Data Fig. 1), during which large shifts of global climate since the Last Glacial Maximum (LGM) are ideal test beds to assess the controls on Great Plains MCS activity and hydroclimate. Furthermore, the site is uniquely sensitive to changes in hydroclimate and MCS activity; nearly 70% of the warm-season precipitation is derived from MCS storms[1], and the site is located on a steep hydroclimatic and ecological gradient between the southwestern subtropical grasslands and the temperate forests of the southeast United States (Extended Data Fig. 2).

In this article, we simultaneously reconstruct past changes in MCS activity, climate and associated vegetation using three independent proxies. First, we analyse the hydrogen isotope composition of sedimentary plant waxes (δD_{wax}) and use it as a proxy for MCS-driven rainfall activity. This interpretation is based on observations of modern precipitation over central Texas, which demonstrates that the stable isotopic composition of rainfall is largely controlled by changes in MCS activity rather than precipitation amount[11,12]. These isotopic changes are preserved in δD_{wax}, providing a proxy record of past changes in MCS activity[13] (see Supplementary Information for details). Our interpretation of δD_{wax} is complemented by our analysis of titanium concentration (%Ti), which reflects enhanced erosion of terrigenous sediment into the cave during extreme rainfall events. Hall's Cave consists of a single room with an upslope opening that permits sediment to be washed into the cave during rainstorms. Although the sediment stratigraphy is probably complex near the cave entrance, our sampling location deeper in the cave receives terrigenous material only during events associated with extreme storms.

Finally, we reconstruct past vegetation changes from carbon isotopic composition of bulk sedimentary organic matter ($\delta^{13}C_{OM}$), which we interpret as reflecting changes in hydroclimate on the basis of modern vegetation–climate relationships. Plants using the C_4 photosynthetic pathway have higher water use efficiency, higher $\delta^{13}C$ values (−9 to −14‰) and are characteristic of savannas and semi-arid grasslands, whereas C_3 plants, including most woody shrubs, trees and winter grasses, have lower $\delta^{13}C$ values (−25 to

[1]Department of Geological Sciences, The University of Texas at Austin, Austin, TX, USA. [2]Institute for Geophysics, The University of Texas at Austin, Austin, TX, USA. [3]Atmospheric and Oceanic Sciences, University of Colorado Boulder, Boulder, CO, USA. [4]School of Earth and Sustainability, Northern Arizona University, Flagstaff, AZ, USA. [5]Instituto de Geología, Universidad Nacional Autónoma de México, Ciudad Universitaria, Mexico City, Mexico. ✉e-mail: chijunsun@ucar.edu

−29‰) and are associated with cooler and wetter environments[14]. Our $\delta^{13}C_{OM}$ record strongly agrees with the previously reported pollen record from Hall's Cave[15] (Extended Data Fig. 3), thus providing a high-resolution record of landscape-scale vegetation cover associated with past changes in hydroclimate.

The δD_{wax}, %Ti and $\delta^{13}C_{OM}$ records from Hall's Cave show remarkably coherent changes over the past 20,000 years (Fig. 1). The consistency between these independent, but complementary, proxies provides a robust record of past climate changes and suggests that there are strong linkages between changes in large-scale convection, extreme precipitation, and ecology. More-arid conditions occur during the late glacial (~20–15 thousand years ago (ka)), with higher $\delta^{13}C_{OM}$ values (−8 to −10‰) indicating a C_4 grass-dominated landscape and more positive δD_{wax} values and low %Ti suggesting reduced MCS activity. At ~14.5 ka, all three proxies change abruptly, reflecting a rapid increase in MCS activity and the establishment of overall wetter conditions. This initial deglacial intensification of MCS activity is terminated by a gradual return to drier, less stormy conditions in the early to mid-Holocene (11–7 ka). Wetter conditions and greater MCS activity return gradually in the late Holocene.

MCS variability dynamically driven by the LLJ

To better understand the controls on these hydroclimatic changes, we compare the proxy reconstructions from Hall's Cave with the transient simulation of climate evolution over the past 21,000 years (TraCE-21ka)[16]. This simulation, conducted using the Community Climate System Model version 3, includes transient changes in greenhouse gas concentrations, orbital insolation and waning/collapsing continental ice sheets, including their effect on coastlines via changes in sea level, as well as freshwater fluxes into the ocean[16]. Because the climate model used in this simulation inadequately represents MCS activity due to its coarse atmospheric resolution (~3.75°), here we explore changes in the large-scale dynamics favouring the development of warm-season convective activity (the springtime LLJ and mid-latitude baroclinic waves)[1] rather than precipitation. We focus on the spring (March to May) because MCSs are most intense and frequent in spring due to the strong coupling between the LLJ and mid-latitude baroclinic forcing[1]. Although the LLJ is also enhanced in summer, the weak summertime baroclinic forcing due to a reduced meridional temperature gradient is unfavourable for the development of large MCSs, and therefore summer is generally dry in the southern and central Great Plains. Here we define an index of LLJ intensity, quantified as the southerly wind at 850 hPa level averaged over the 95–103° W, 22–34° N domain, which is selected on the basis of the location of the maximum southerly flow in the model (see Supplementary Information for details). The GCM used in the TraCE-21ka simulation realistically reproduces the seasonal development and spatial extent of the southerly LLJ (Supplementary Information), making it a suitable metric to diagnose the drivers of past MCS variability over the central United States. In addition to the LLJ, we assess changes in baroclinic forcing via computing the eddy kinetic energy, which reflects the position of the mid-latitude storm tracks (Supplementary Information).

The temporal evolution of the simulated LLJ intensity shows striking similarities to our multiproxy reconstructions of past MCS activity and vegetation change from Hall's Cave, including a weaker-than-present springtime LLJ at the LGM, an abrupt intensification starting at around 13.9 ka, a subsequent gradual weakening of the LLJ during the early to mid-Holocene and a gradual strengthening of the LLJ after ~5 ka (Fig. 1). During the LGM, the North American ice sheets expanded, cooling the continental interior and leading to the development of anomalous high pressure over the central United States. This weakens the zonal pressure gradient between the central United States and the Atlantic, reducing the strength of the geostrophic LLJ winds and causing the LLJ to turn

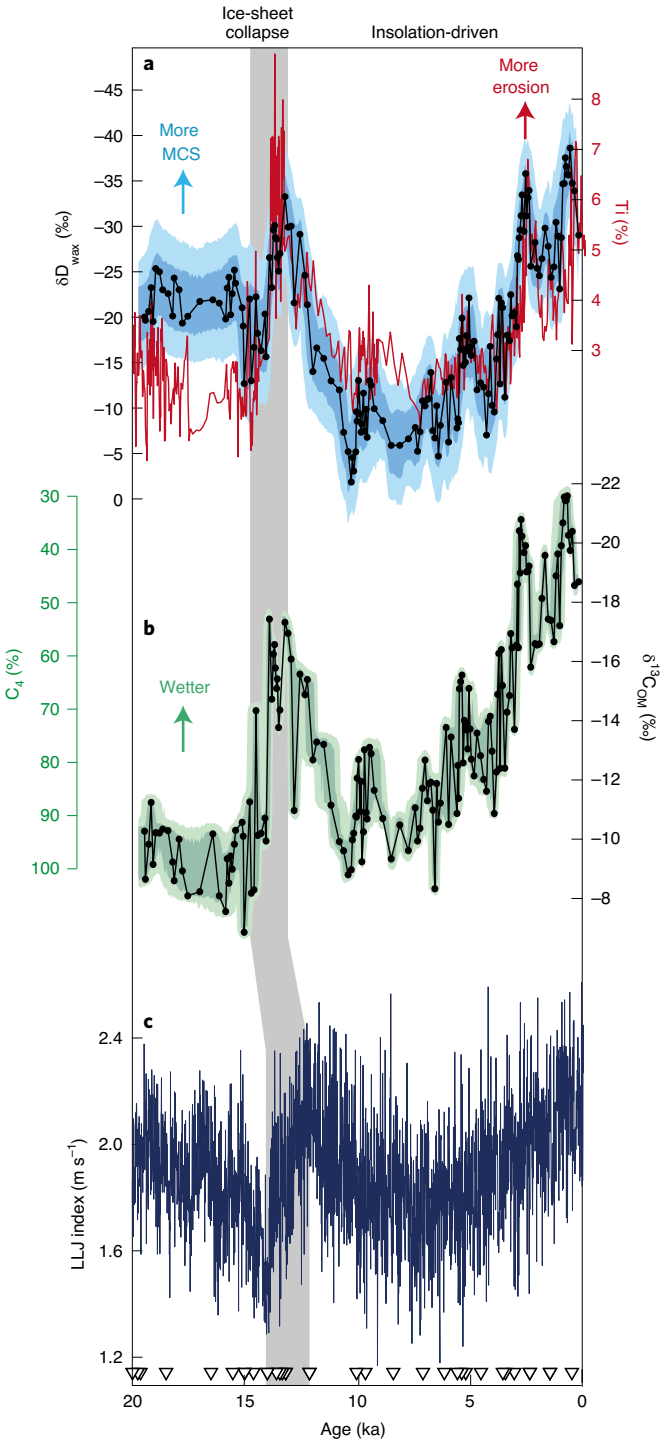

Fig. 1 | Proxy records generated in this study compared with the simulated evolution of the LLJ in the TraCE-21ka experiment. **a**, Records of δD_{wax} and %Ti at Hall's Cave, interpreted as changes in MCS and soil erosion from intense precipitation, respectively. δD_{wax} is corrected for vegetation and ice volume (Methods). **b**, $\delta^{13}C_{OM}$ at Hall's Cave, interpreted as changes in the relative abundance of C_3 and C_4 vegetation. **c**, Springtime LLJ index in TraCE-21ka. Shadings on the reconstructions reflect 1σ (dark) and 2σ (light) uncertainties. Triangles at the bottom denote radiocarbon dates. The timing of the largest ice volume change in TraCE-21ka was prescribed at 13.9 ka to match other boundary condition changes, trailing the estimates from updated deglacial chronologies (Supplementary Information).

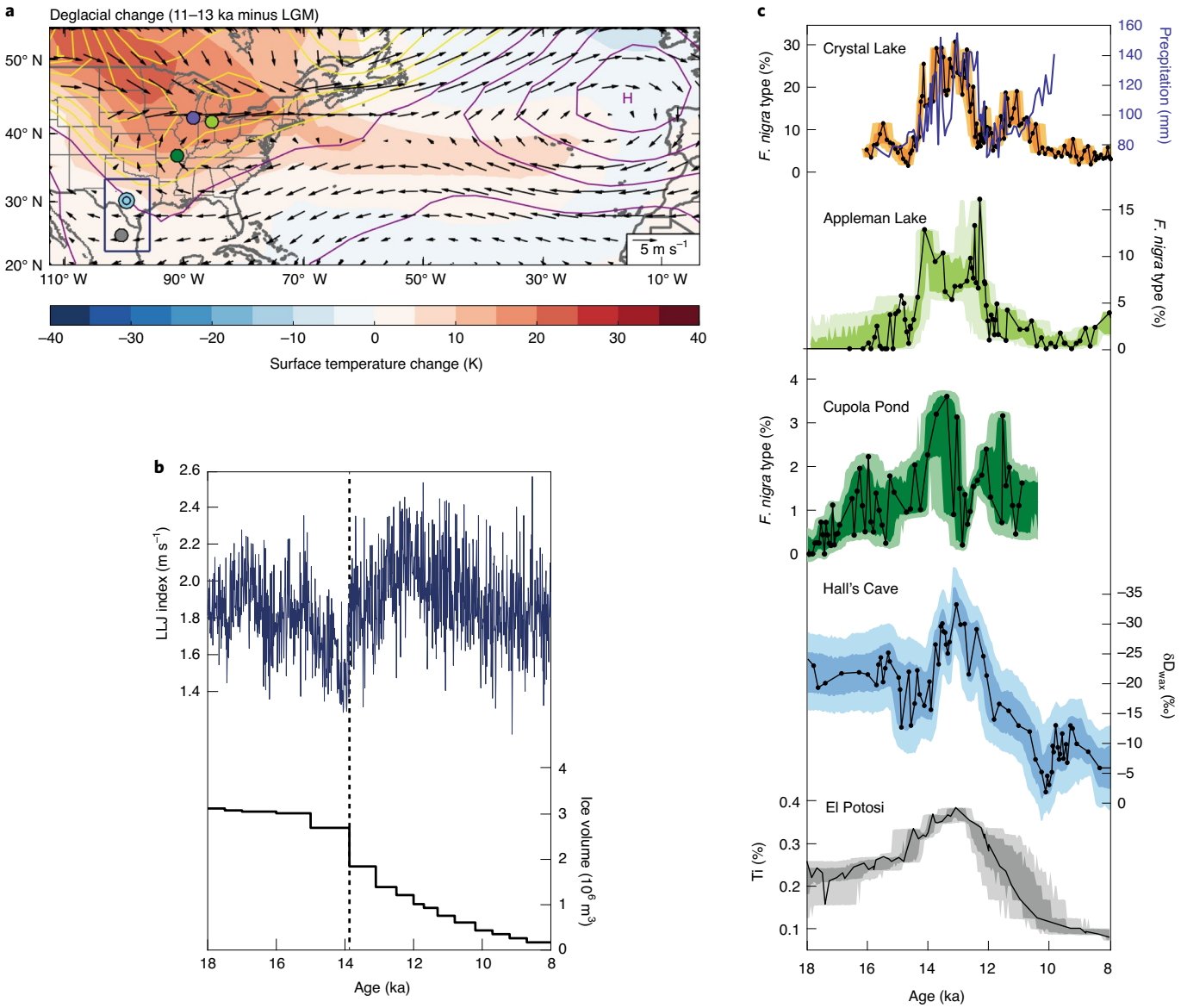

Fig. 2 | Deglacial hydroclimate change associated with ice-sheet 'saddle collapse'. a, Changes in springtime (March to May) surface air temperature (shadings), sea-level pressure (contours; yellow, negative values; purple, positive values; contour interval, 2 hPa) and 850 hPa winds (vectors) during 11–13 ka relative to the LGM, showing strong warming over North America, a steepened zonal pressure gradient and an intensified LLJ. Coloured dots correspond to the site locations of the palaeoclimate records shown with the same colours in **c**. The dark blue rectangle indicates the area used to define the LLJ index. H, high pressure anomaly over the Atlantic; L, low pressure anomaly over land. **b**, Simulated changes in the springtime LLJ and prescribed changes in the North American ice sheets in TraCE-21ka. The dashed line marks the timing of the saddle collapse in TraCE-21ka. **c**, Palaeohydrologic records across the Great Plains showing a deglacial hydrologic signal (see Supplementary Information for details). Shadings indicate 1σ (dark) and 2σ (light) uncertainties based on analytical and age model errors.

eastwards (Extended Data Fig. 4). Given the strong dynamical control of the LLJ on MCS development in this region, a weaker LLJ should result in weaker or less-frequent storms, consistent with the δD and %Ti data from Hall's Cave. Although reduced rainfall and storm activity during the LGM could also occur because of the thermodynamic effects associated with an ice-sheet-driven southward displacement of the jet stream[17–21], which ventilates cold dry air into the region[22,23], this response should also strengthen the baroclinic forcing over the southern Great Plains, making conditions more favourable for MCS genesis. Thus, a dynamical control of MCS variability via changes in LLJ intensity, driven primarily by continental land surface temperatures, is the more likely explanation for weaker MCS activity and more-arid conditions during the LGM than is a thermodynamic forcing associated with ventilation. In addition, LLJ intensity as a dominant driver of changes in MCS activity has been provoked to explain millennial-scale southern Great Plains MCS variability during the Marine Isotope Stage 3 (27.8–59.5 ka)[12].

Springtime warming drives changes in LLJ intensity

The simulated deglacial intensification of the LLJ is remarkably similar to the rapid increase in MCS activity and the expansion of C_3 vegetation reconstructed from Hall's Cave (Fig. 1). In the model, strengthening of the LLJ at this time is caused by the enhancement of the zonal pressure gradient across central North America due to a combination of land surface warming and remote forcing of the North Atlantic subtropical high. Laurentide ice-sheet collapse

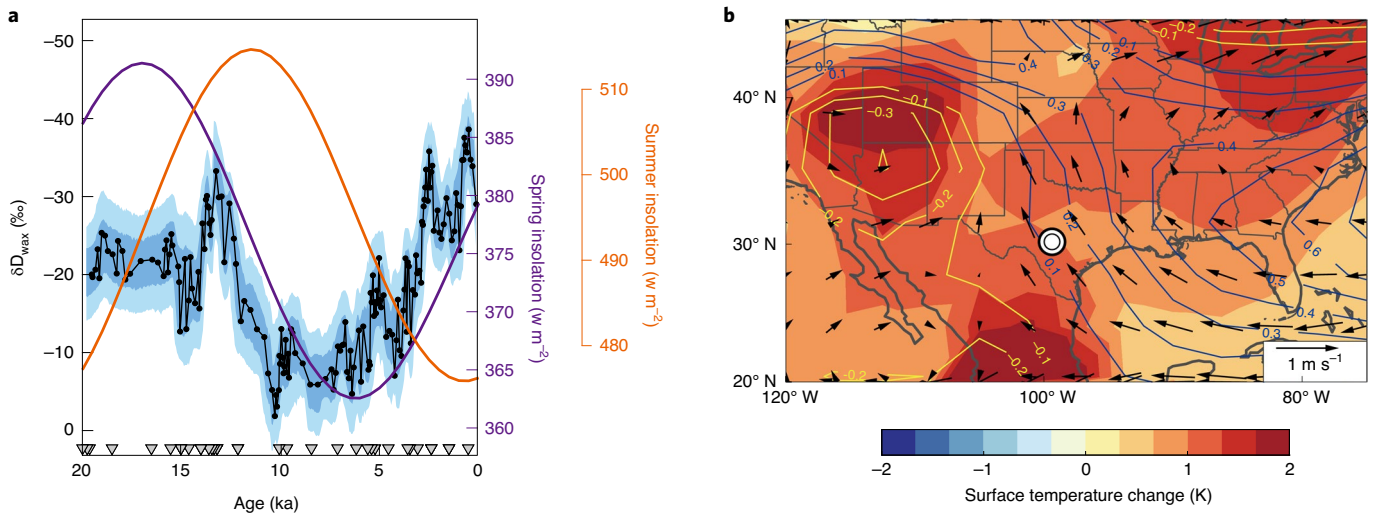

Fig. 3 | Insolation-driven changes in hydroclimate during the Holocene. a, Hall's Cave δD_{wax} and changes in spring (21 March, purple) and summer (21 June, orange) insolation at 30° N. Shadings indicate 1σ (dark) and 2σ (light) uncertainties based on analytical and age model errors. **b**, Changes in springtime surface temperature (shadings), sea-level pressure (contours; yellow, negative values; blue, positive values; unit, mbar) and 850 hPa wind (vectors) during the late Holocene (0 ka minus 6 ka). White circles indicate the location of Hall's Cave.

results in land surface warming and the development of anomalous low pressure along the southern margin of the ice sheet, across the northern Great Plains and the Great Lakes region, largely as a result of changes in land surface albedo (Fig. 2a and Extended Data Fig. 5). At the same time, the North Atlantic subtropical high strengthens as a result of topographic forcing associated with the Laurentide ice-sheet collapse (Fig. 2a)[24–26]. Together, these responses steepen the zonal pressure gradient, intensifying the geostrophic LLJ (Fig. 2a). This suggests that as the ice sheet retreats, the LLJ responds dynamically by strengthening in response to land surface warming over the Great Plains, which could account for the enhanced MCS activity inferred from our reconstruction. Proxy hydroclimate and vegetation records from across central United States show a similar abrupt change at this time[27–30] (Fig. 2c and Extended Data Fig. 6), supporting the hypothesis that this change reflects a change in regional atmospheric dynamics associated with the deglacial intensification of the LLJ. In addition to the strengthened LLJ, the abrupt increase in MCS activity at this time could have been driven by enhanced frontal variability associated with a more variable jet stream as the Laurentide ice sheet retreated. However, this shift occurred progressively through the deglaciation (Extended Data Fig. 4) and thus cannot explain the rather abrupt change recorded by the proxies. Furthermore, the proxy reconstruction indicates that MCS activity subsequently declined in the early Holocene, consistent with simulated changes in the LLJ, while eddy activity remained strong, suggesting a dominant role for the LLJ in MCS generation.

In the TraCE-21ka simulation, this transition initiates at 13.9 ka, in conjunction with the separation of the Cordilleran and Laurentide ice sheets (the saddle collapse)[31]. We note that the abrupt change in the proxy records occurs slightly earlier than in the model (~14.5 ka at Hall's Cave). However, the earlier timing in the proxy records is consistent with updated estimates from North American deglacial chronologies[32], which indicate that the separation occurred at about 14.1–14.6 ka and that the ice-sheet changes were prescribed too late in the transient simulations (Supplementary Information). Support for the dominant role of ice collapse in driving this response, rather than global climate changes associated with the Bølling–Allerød warming (14.9 ka), is from the TraCE-21ka single-forcing experiments, which show the same behaviour in ice-sheet-only simulations (Supplementary Information and Extended Data Fig. 7).

Following initial strengthening of the LLJ associated with ice-sheet collapse and progressing into the Holocene, land surface temperature changes driven by gradual changes in Northern Hemisphere insolation modulate the intensity of the LLJ. After the initial strengthening at 13.9 ka, the simulated LLJ decreases gradually from ~12 ka to the mid-Holocene (~5–7 ka) and then increases towards the present following changes in spring insolation (Fig. 3a). In the model, decreased early to mid-Holocene insolation cools the land surface relative to the ocean, increasing surface pressure over the southern Rockies and central Great Plains and weakening the LLJ. As spring insolation gradually increases towards the late Holocene (5–0 ka), warming of the land surface strengthens the springtime LLJ (Fig. 3b).

Support for springtime insolation changes as the dominant driver of Holocene changes in the LLJ comes from the strong agreement between the timing of changes in proxy-reconstructed MCS activity, spring insolation and the associated changes in springtime LLJ activity in TraCE-21ka (Fig. 3a). By contrast, summer or integrated warm-season insolation changes peak earlier and produce a stronger LLJ in the early to mid-Holocene, inconsistent with the observed changes in hydroclimate and MCS activity evident at Hall's Cave. Additional support comes from modern observations; while the LLJ responds to land surface warming and the development of zonal pressure gradient anomalies seasonally, MCS activity is predominantly associated with springtime land surface conditions because little rainfall occurs in the summer when weak large-scale baroclinicity is unfavourable for MCS genesis, irrespective of the strength of the LLJ[1]. In fact, this mechanism, whereby springtime land surface warming is critical for seasonal changes in LLJ intensity, is evident across mid-Holocene climate simulations performed as part of the Paleoclimate Modeling Intercomparison Project (PMIP3)[33] and explains drier mid-Holocene conditions in the central United States at that time[15,34–37], despite the maxima in summertime insolation (Extended Data Fig. 8).

Although there is good agreement between the model-inferred changes in LLJ intensity and proxy reconstruction of MCS activity throughout the record, a notable difference occurs in the late Holocene, when the magnitude of changes in the proxy record appears to be much larger than the glacial changes, despite the relatively smaller changes in the LLJ simulated by the model. This

suggests that other factors could have influenced the late Holocene climate response. Given the critical role of springtime land surface warming in driving LLJ variability and the dramatic changes in vegetation cover during this period, we hypothesize that the differences in the magnitude of the late Holocene response may reflect an influence from land surface feedbacks on MCS intensity. A replacement of C_4 grasslands by C_3 forests may act both to further intensify the LLJ through enhanced land surface warming via the albedo effect and to provide boundary layer instability via increased evapotranspiration[38]. Such land surface feedbacks are known to play an important role in modulating warm-season temperature and precipitation today[39–41], although they are not sufficiently represented in the current generation of GCMs[42] and, as a result, are probably underestimated in the simulations examined here.

The palaeoclimatic reconstruction from Hall's Cave provides robust evidence for a highly sensitive climate system in the central United States dominated by changes in springtime MCSs. The similarities between proxy reconstructions of MCS behaviour and vegetation further suggest that these changes in convective storm development also drive large-scale ecosystem changes. While state-of-the-art GCMs are unable to accurately represent storm systems such as MCSs, the remarkable similarities between changes in proxy-reconstructed MCS behaviour and simulations of the springtime LLJ support the dominant dynamical control of the seasonal changes in LLJ strength on the development of convective storms over the Great Plains over the past 20 kyr. In the simulations, these changes in LLJ activity are forced by springtime land surface temperature changes over the central Great Plains. This result is consistent with observed increases in LLJ strength and MCS activity in response to global warming over the past three decades[4] and with the results of the Coupled Model Intercomparison Project phases 5 and 6, which consistently predict a strengthened springtime LLJ in response to future global warming[43,44]. Together, these results indicate that dynamic impacts of the LLJ have dominated the response of the Great Plains hydroclimate system for the past 20 kyr and will lead to an increased risk of extreme weather in response to future warming.

Online content

Any methods, additional references, Nature Research reporting summaries, source data, extended data, supplementary information, acknowledgements, peer review information; details of author contributions and competing interests; and statements of data and code availability are available at https://doi.org/10.1038/s41561-021-00860-8.

Received: 11 September 2020; Accepted: 28 October 2021;
Published online: 29 November 2021

References

1. Feng, Z. et al. Spatiotemporal characteristics and large-scale environments of mesoscale convective systems east of the Rocky Mountains. *J. Clim.* **32**, 7303–7328 (2019).
2. Kousky, C. Informing climate adaptation: a review of the economic costs of natural disasters. *Energy Econ.* **46**, 576–592 (2014).
3. Schumacher, R. S. & Johnson, R. H. Characteristics of US extreme rain events during 1999–2003. *Weather Forecast.* **21**, 69–85 (2006).
4. Feng, Z. et al. More frequent intense and long-lived storms dominate the springtime trend in central US rainfall. *Nat. Commun.* **7**, 13429 (2016).
5. Maloney, E. D. et al. North American climate in CMIP5 experiments: part III: assessment of twenty-first-century projections. *J. Clim.* **27**, 2230–2270 (2014).
6. Cook, K. H., Vizy, E. K., Launer, Z. S. & Patricola, C. M. Springtime intensification of the Great Plains low-level jet and Midwest precipitation in GCM simulations of the twenty-first century. *J. Clim.* **21**, 6321–6340 (2008).
7. Harding, K. J. & Snyder, P. K. Examining future changes in the character of central US warm-season precipitation using dynamical downscaling. *J. Geophys. Res. Atmos.* **119**, 13116–13136 (2014).
8. Christensen, J. H. et al. in *Climate Change 2013: The Physical Science Basis* (eds Stocker, T. F. et al.) 1217–1308 (IPCC, Cambridge Univ. Press, 2013).
9. Pfahl, S., O'Gorman, P. A. & Fischer, E. M. Understanding the regional pattern of projected future changes in extreme precipitation. *Nat. Clim. Change* **7**, 423–427 (2017).
10. Song, F., Leung, L. R., Lu, J. & Dong, L. Future changes in seasonality of the North Pacific and North Atlantic subtropical highs. *Geophys. Res. Lett.* **45**, 11959–11968 (2018).
11. Sun, C., Shanahan, T. M. & Partin, J. Controls on the isotopic composition of precipitation in the south-central United States. *J. Geophys. Res. Atmos.* **124**, 8320–8335 (2019).
12. Maupin, C. R. et al. Abrupt southern Great Plains thunderstorm shifts linked to glacial climate variability. *Nat. Geosci.* **14**, 396–401 (2021).
13. Sachse, D. et al. Molecular paleohydrology: interpreting the hydrogen-isotopic composition of lipid biomarkers from photosynthesizing organisms. *Annu. Rev. Earth Planet. Sci.* **40**, 221–249 (2012).
14. Boutton, T. W., Archer, S. R., Midwood, A. J., Zitzer, S. F. & Bol, R. $\delta^{13}C$ values of soil organic carbon and their use in documenting vegetation change in a subtropical savanna ecosystem. *Geoderma* **82**, 5–41 (1998).
15. Cordova, C. E. & Johnson, W. C. An 18 ka to present pollen- and phytolith-based vegetation reconstruction from Hall's Cave, south-central Texas, USA. *Quat. Res.* **92**, 497–518 (2019).
16. Liu, Z. et al. Transient simulation of last deglaciation with a new mechanism for Bolling–Allerød warming. *Science* **325**, 310–314 (2009).
17. COHMAP Members Climatic changes of the last 18,000 years: observations and model simulations. *Science* **241**, 1043–1052 (1988).
18. Oster, J. L., Ibarra, D. E., Winnick, M. J. & Maher, K. Steering of westerly storms over western North America at the Last Glacial Maximum. *Nat. Geosci.* **8**, 201–205 (2015).
19. Lora, J. M., Mitchell, J. L. & Tripati, A. E. Abrupt reorganization of North Pacific and western North American climate during the last deglaciation. *Geophys. Res. Lett.* **43**, 11796–11804 (2016).
20. Lora, J. M. Components and mechanisms of hydrologic cycle changes over North America at the Last Glacial Maximum. *J. Clim.* **31**, 7035–7051 (2018).
21. Conroy, J. L., Karamperidou, C., Grimley, D. A. & Guenthner, W. R. Surface winds across eastern and midcontinental North America during the Last Glacial Maximum: a new data–model assessment. *Quat. Sci. Rev.* **220**, 14–29 (2019).
22. Bhattacharya, T., Tierney, J. E. & DiNezio, P. Glacial reduction of the North American monsoon via surface cooling and atmospheric ventilation. *Geophys. Res. Lett.* **44**, 5113–5122 (2017).
23. Chou, C. & Neelin, J. D. Mechanisms limiting the northward extent of the northern summer monsoons over North America, Asia, and Africa. *J. Clim.* **16**, 406–425 (2003).
24. Cook, K. H. & Held, I. M. Stationary waves of the Ice Age climate. *J. Clim.* **1**, 807–819 (1988).
25. Löfverström, M., Caballero, R., Nilsson, J. & Kleman, J. Evolution of the large-scale atmospheric circulation in response to changing ice sheets over the last glacial cycle. *Climate* **10**, 1453–1471 (2014).
26. Roberts, W. H. G., Li, C. & Valdes, P. J. The mechanisms that determine the response of the Northern Hemisphere's stationary waves to North American ice sheets. *J. Clim.* **32**, 3917–3940 (2019).
27. Gonzales, L. M., Williams, J. W. & Grimm, E. C. Expanded response-surfaces: a new method to reconstruct paleoclimates from fossil pollen assemblages that lack modern analogues. *Quat. Sci. Rev.* **28**, 3315–3332 (2009).
28. Gill, J. L., Williams, J. W., Jackson, S. T., Lininger, K. B. & Robinson, G. S. Pleistocene megafaunal collapse, novel plant communities, and enhanced fire regimes in North America. *Science* **326**, 1100–1103 (2009).
29. Jones, R. A., Williams, J. W. & Jackson, S. T. Vegetation history since the Last Glacial Maximum in the Ozark Highlands (USA): a new record from Cupola Pond, Missouri. *Quat. Sci. Rev.* **170**, 174–187 (2017).
30. Roy, P. D. et al. Atlantic Ocean modulated hydroclimate of the subtropical northeastern Mexico since the Last Glacial Maximum and comparison with the southern US. *Earth Planet. Sci. Lett.* **434**, 141–150 (2016).
31. Gregoire, L. J., Payne, A. J. & Valdes, P. J. Deglacial rapid sea level rises caused by ice-sheet saddle collapses. *Nature* **487**, 219–222 (2012).
32. Tarasov, L., Dyke, A. S., Neal, R. M. & Peltier, W. R. A data-calibrated distribution of deglacial chronologies for the North American ice complex from glaciological modeling. *Earth Planet. Sci. Lett.* **315–316**, 30–40 (2012).
33. Braconnot, P. et al. Evaluation of climate models using palaeoclimatic data. *Nat. Clim. Change* **2**, 417–424 (2012).
34. Nordt, L., Von Fischer, J., Tieszen, L. & Tubbs, J. Coherent changes in relative C_4 plant productivity and climate during the late Quaternary in the North American Great Plains. *Quat. Sci. Rev.* **27**, 1600–1611 (2008).
35. Williams, J. W., Shuman, B., Bartlein, P. J., Diffenbaugh, N. S. & Webb, T. III Rapid, time-transgressive, and variable responses to early Holocene midcontinental drying in North America. *Geology* **38**, 135–138 (2010).
36. Shuman, B. N. & Marsicek, J. The structure of Holocene climate change in mid-latitude North America. *Quat. Sci. Rev.* **141**, 38–51 (2016).

37. Skinner, C. B., Lora, J. M., Payne, A. E. & Poulsen, C. J. Atmospheric river changes shaped mid-latitude hydroclimate since the mid-Holocene. *Earth Planet. Sci. Lett.* **541**, 116293 (2020).
38. Liu, Z., Notaro, M., Kutzbach, J. & Liu, N. Assessing global vegetation–climate feedbacks from observations. *J. Clim.* **19**, 787–814 (2006).
39. Koster, R. D. Regions of strong coupling between soil moisture and precipitation. *Science* **305**, 1138–1140 (2004).
40. Dirmeyer, P. A. The terrestrial segment of soil moisture–climate coupling. *Geophys. Res. Lett.* **38**, L16702 (2011).
41. Al-Yaari, A., Ducharne, A., Cheruy, F., Crow, W. T. & Wigneron, J. P. Satellite-based soil moisture provides missing link between summertime precipitation and surface temperature biases in CMIP5 simulations over conterminous United States. *Sci. Rep.* **9**, 1657 (2019).
42. Jiang, X., Niu, G.-Y. & Yang, Z.-L. Impacts of vegetation and groundwater dynamics on warm season precipitation over the central United States. *J. Geophys. Res.* https://doi.org/10.1029/2008jd010756 (2009).
43. Tang, Y. et al. Future changes in the climatology of the Great Plains low-level jet derived from fine resolution multi-model simulations. *Sci. Rep.* **7**, 5029 (2017).
44. Zhou, W., Leung, L. R., Song, F. & Lu, J. Future changes in the Great Plains low-level jet governed by seasonally dependent pattern changes in the North Atlantic subtropical high. *Geophys. Res. Lett.* **48**, e2020GL090356 (2021).

Methods

Site location. Hall's Cave is a small, open limestone cave located on the Edwards Plateau in central Texas (30.14° N, 99.53° W, 695 m, Extended Data Fig. 2). The cave consists of a single chamber (30 × 55 m) formed in the Segovia Member of the Lower Cretaceous Edwards limestone and contains 3.7 metres of well-stratified, fossiliferous sediments[45]. The cave sediments comprise clays, fine-grained sands and limestone clasts either washed into the cave from the entrance during large storm events or broken from cave walls. Organic matter in the cave is probably composed of a combination of terrigenous organic matter washed into the cave, bat guano and owl pellets. The complete stratigraphy has previously been described in detail by Toomey[45] and updated recently by Cordova and Johnson[15]. The sediments contained in the cave have been used to understand the regional changes in vegetation, faunal assemblage and soil erosion of the past 20 kyr, for example, refs. [15,45–49].

Sampling. Previous sampling of the sediment record from Hall's Cave was conducted by Toomey[45] via a series of sediment pits. To obtain high-resolution, continuous sediment records for this study, we collected additional samples by coring approximately 10 cm from the northwest edge of Toomey's pit 1 d/e in January 2012. Cores were taken in overlapping adjacent 20–25 cm segments because of the presence of limestone clasts that made penetration difficult. By taking short overlapping core sections, we were able to collect a continuous sediment record, despite the presence of limestone cobbles at some depths. During our first visit, large limestone clasts limited penetration to a depth of ~1 m, so a second core, reaching a depth of ~3 m, was collected during a subsequent trip in June 2012, approximately 10 cm from the first coring location. To correlate between our sediment record, the record of Toomey[45] and the radiocarbon chronology of Cooke et al.[47], we traced distinct lithological changes in our sediment record to markers left in the side of the excavation pit by Cooke[47]. Depth correlations were confirmed with a plumb line extended from a datum left by Toomey[45].

Age model and uncertainty propagation. Chronological control for the cave sediment record from Hall's Cave is based on 37 previously published accelerator mass spectrometry ^{14}C measurements made primarily on collagen extracted from fossil bones preserved in the cave sediments (Supplementary Table 1). Age–depth modelling was performed using the Bayesian age–depth modelling programme BACON[50] and the IntCal13 radiocarbon calibration curve[51]. BACON models the age–depth relationship assuming a gamma probability distribution for accumulation rates and using the true (non-normal) calibrated ^{14}C age distributions. The final product is a population of geologically realistic age–depth models, which reflects the uncertainties in the analytical radiocarbon age measurements as well as in the calibrated ages (Extended Data Fig. 1).

Carbon isotope analysis of $\delta^{13}C_{OM}$. Samples were taken continuously at 1 cm intervals (equivalent to ~59 ± 49 yr) over the entire record. Sediment samples were freeze-dried and homogenized with a mortar and pestle. Then 2–20 mg of sediment was weighed into silver capsules and acidified with sulfurous acid to remove inorganic carbon[52]. Before analysis, samples were dried at 70 °C for 48 hours. Carbon isotope analysis of bulk organic matter was performed by combustion in an elemental analyser (Costech Instruments Elemental Combustion System 4010) coupled to an isotope ratio mass spectrometer (Thermo Scientific Delta V Plus). The analytical precision of these analyses was 0.24‰ based on repeated measurements of an in-house standard.

Lipid extraction. A total of 20–50 g of sediment was freeze-dried, ground and homogenized with a mortar and pestle, and extracted via microwave solvent extraction (CEM MARS) with dichloromethane/methanol (v/v: 9/1). Extracts were filtered and dried over sodium sulfate and then separated into neutral and polar fractions over deactivated silica gel using hexane and dichloromethane/methanol (v/v: 9/1). The neutral fraction was additionally separated into adduct and non-adduct fractions by urea adduction to isolate the straight-chain compounds for further analysis.

Hydrogen isotope analysis of δD_{wax}. Hydrogen isotope analysis of individual *n*-alkanes was performed using a TRACE gas chromatograph operated in splitless mode and equipped with a DB-5ms column (30 m/0.25 µm/0.25 mm; length/film thickness/inner diameter), coupled to a Delta V isotope ratio mass spectrometer via a pyrolysis interface operated at 1,430 °C. The H_3^+ factors were determined daily, and external isotope standards (either the B_2 *n*-alkane or F_8 FAME mix, Indiana University Biogeochemical Laboratories) were measured between every five samples. The external standards had a precision of <±5‰. Co-injection of propane during the analysis of the external standards allowed us to determine the isotope value of our propane reference tank and allowed us to use the propane as an internal standard within each unknown sample analysis. Between three and five propane injections were performed during each sample run. Within each run, the propane peaks had a precision of <±5‰. Most samples were run in either duplicate or triplicate, and the standard deviations based on replicate analysis of the same samples were <±5‰. Here we report data from the C_{27} *n*-alkane, which was the most abundant compound in most of the samples and had the best chromatographic separation from interfering peaks.

It has been shown that isotope fractionation during biosynthesis is slightly different between C_3 and C_4 plants[13]. Because the $\delta^{13}C$ record from Hall's Cave indicates that there were substantial changes in the proportion of C_3 and C_4 plants, particularly during the mid- to late Holocene, the δD_{wax} record needs to be corrected for the influence of plant-specific hydrogen isotope fractionation. Therefore, following other workers[53], we used changes in C_3/C_4 plant abundances estimated from $\delta^{13}C_{OM}$ to make this correction. We assumed that $\delta^{13}C_{OM}$ reflects a linear mixing between C_3 and C_4 plants with endmember $\delta^{13}C$ values of −27‰ and −9‰, respectively (Supplementary Information). We then used reported values for the apparent hydrogen isotope fractionation (ε) in C_4 grasses (−134 ± 15‰) and C_3 trees and shrubs (−113 ± 5‰)[13] to compute the hydrogen isotope composition of source water (δD_{sw}).

$$\delta D_{sw} = \left[\frac{\delta D_{wax} + 1,000}{\left(\frac{\varepsilon}{1,000}\right) + 1} \right] - 1,000 \quad (1)$$

Another important influence on the hydrogen isotope composition of precipitation is associated with changes in source-water composition resulting from changes in global ice volume. In this study, we adjusted for the influence of these changes on our record by assuming a 1‰ increase in the $\delta^{18}O$ of the global ocean during the LGM and generate a millennial-resolution time series of changes in $\delta^{18}O_{ocean}$ using the LR04 benthic oxygen isotope stack[54]. We converted the changes in $\delta^{18}O$ to a change in the δD of the glacial ocean, assuming that the deuterium excess of the ocean was zero[53,55], and subtracted the δD_{ocean} values from the measured δD_{wax} to produce an adjusted δD_{wax} curve.

In situ XRF analysis of major and trace element concentrations. A record of %Ti abundance was generated by energy-dispersive X-ray fluorescence (ED-XRF) using a Niton FXL 950 portable XRF analyser equipped with an Ag X-ray tube. Before analysis, the sediment core was subsampled, samples were dried at 50 °C, sieved to remove the >0.5 mm fraction and homogenized with an agate mortar and pestle. Sieving was necessary to remove the largest lithic fragments derived from within the cave as well as bone fragments and to focus on the fine fraction washed into the cave during storm events. After homogenization, all samples were hand pressed to a uniform density before analysis. Each sample was analysed for 60 s in triplicate. Major element concentrations were corrected using a set of three sediment reference materials (SRM-2702, sdAR-M2 and SRM-2709a)[56]. The standard deviation on seven replicate analyses of the reference materials was <3% for the major elements, including Ti.

Climate model experiments. We analysed the model output of the Transient Climate Simulations of the Last 21,000 Years experiment[16], performed with the fully coupled Community Climate System Model version 3 at the National Center for Atmospheric Research (NCAR). The atmospheric data were downloaded from the Climate Data Gateway at NCAR (https://www.earthsystemgrid.org/). TraCE-21ka was simulated with time-evolving external forcings, including orbital parameters, concentrations of greenhouse gases, continental ice sheets and meltwater fluxes. In addition to the full TraCE-21ka simulation, we analysed the model output from the single-forcing experiments of TraCE-21ka, where only one of the external forcings (ice-sheet volume, greenhouse gas, insolation, meltwater flux) was prescribed to change as in the full simulation, whereas the rest of these parameters were kept at their LGM levels[57,58]. Last, we used the mid-Holocene (6 ka) and pre-Industrial (0 ka) experiments available through the PMIP3[33]. These PMIP3 simulations share a common PMIP3 protocol for boundary conditions and use interactive carbon cycle. The vegetation and land surface are either computed using a dynamical vegetation module or prescribed as in pre-Industrial. More details are provided in Supplementary Information.

Data availability

All geochemical data generated for this study are available for download from the National Oceanic and Atmospheric Administration National Centers for Environmental Information Paleoclimatology archive (https://www.ncei.noaa.gov/access/paleo-search/study/34492) and are also available from the Supplementary Data file of the online version of this paper. Model outputs from the TraCE-21ka experiments, including full and single-forcing simulations, were downloaded from the Earth System Grid website (https://www.earthsystemgrid.org/project/trace.html).

References

45. Toomey, R. S. *Late Pleistocene and Holocene Faunal and Environmental Changes at Hall's Cave, Kerr County, Texas*. PhD dissertation, Univ. Texas Austin (1993).
46. Ellwood, B. B. & Gose, W. A. Heinrich H1 and 8200 yr BP climate events recorded in Hall's Cave, Texas. *Geology* https://doi.org/10.1130/g22549.1 (2006).

47. Cooke, M. J. et al. Precise timing and rate of massive late Quaternary soil denudation. *Geology* **31**, 853–856 (2003).
48. Wicks, T. Z., Thirumalai, K., Shanahan, T. M. & Bell, C. J. The use of $\delta^{13}C$ values of leporid teeth as indicators of past vegetation. *Palaeogeogr. Palaeoclimatol. Palaeoecol.* **418**, 245–260 (2015).
49. Bourne, M. D. et al. High-intensity geomagnetic field 'spike' observed at ca. 3000 cal BP in Texas, USA. *Earth Planet. Sci. Lett.* **442**, 80–92 (2016).
50. Blaauw, M. & Christen, J. A. Flexible paleoclimate age–depth models using an autoregressive gamma process. *Bayesian Anal.* **6**, 457–474 (2011).
51. Reimer, P. J. et al. Selection and treatment of data for radiocarbon calibration: an update to the International Calibration (IntCal) criteria. *Radiocarbon* **55**, 1923–1945 (2013).
52. Fernandes, M. & Krull, E. How does acid treatment to remove carbonates affect the isotopic and elemental composition of soils and sediments? *Environ. Chem.* **5**, 33–39 (2008).
53. Shanahan, T. M. et al. The time-transgressive termination of the African Humid Period. *Nat. Geosci.* **8**, 140–144 (2015).
54. Lisiecki, L. E. & Raymo, M. E. A Pliocene-Pleistocene stack of 57 globally distributed benthic $\delta^{18}O$ records. *Paleoceanography* **20**, PA1003 (2005).
55. Tierney, J. E., Russell, J. M., Damsté, J. S. S., Huang, Y. & Verschuren, D. Late Quaternary behavior of the East African monsoon and the importance of the Congo Air Boundary. *Quat. Sci. Rev.* **30**, 798–807 (2011).
56. Quiroz Jiménez, J. D. & Roy, P. D. Evaluation of geochemical data by two different XRF spectrometers in sediments from the Santiaguillo Basin (state of Durango, Mexico). *Geofis. Int.* **56**, 305–315 (2017).
57. He, F. et al. Northern Hemisphere forcing of Southern Hemisphere climate during the last deglaciation. *Nature* **494**, 81–85 (2013).
58. Otto-Bliesner, B. L. et al. Coherent changes of southeastern equatorial and northern African rainfall during the last deglaciation. *Science* **346**, 1223–1227 (2014).
59. Kalnay, E. et al. The NCEP/NCAR 40-year reanalysis project. *Bull. Am. Meteorol. Soc.* **77**, 437–472 (1996).
60. Still, C. et al. *ISLSCP II C4 Vegetation Percentage* (ORNL DAAC, 2009).
61. Kim, H. K. *Late-Glacial and Holocene Environment in Central Iowa: A Comparative Study of Pollen Data from Four Sites.* PhD dissertation, Univ. Iowa (1986).
62. Curry, B. B. *The Late-Glacial and Early Holocene Geology, Paleoecology and Paleohydrology of the Brewster Creek Site, a Proposed Wetland Restoration Site, Pratt's Wayne Woods Forest Preserve and James "Pate" Philip State Park, Bartlett, Illinois* Circular No. 571 (Illinois State Geological Survey, 2007).
63. Saunders, J. J. et al. Paradigms and proboscideans in the southern Great Lakes region, USA. *Quat. Int.* **217**, 175–187 (2010).
64. Wang, H., Stumpf, A. J., Miao, X. & Lowell, T. V. Atmospheric changes in North America during the last deglaciation from dune-wetland records in the Midwestern United States. *Quat. Sci. Rev.* **58**, 124–134 (2012).
65. Gill, J. L., Williams, J. W., Jackson, S. T., Donnelly, J. P. & Schellinger, G. C. Climatic and megaherbivory controls on late-glacial vegetation dynamics: a new, high-resolution, multi-proxy record from Silver Lake, Ohio. *Quat. Sci. Rev.* **34**, 66–80 (2012).
66. Gruger, J. Studies on the late Quaternary vegetation history of northeastern Kansas. *Geol. Soc. Am. Bull.* **84**, 239–250 (1973).
67. Humphrey, J. D. & Ferring, C. R. Stable isotopic evidence for latest Pleistocene and Holocene climatic change in north-central Texas. *Quat. Res.* **41**, 200–213 (1994).
68. Bryant, V. M. Jr A 16,000 year pollen record of vegetational change in central Texas. *Palynology* **1**, 143–156 (1977).
69. Feng, W. et al. Changing amounts and sources of moisture in the US southwest since the Last Glacial Maximum in response to global climate change. *Earth Planet. Sci. Lett.* **401**, 47–56 (2014).
70. Nordt, L. C., Boutton, T. W., Jacob, J. S. & Mandel, R. D. C_4 plant productivity and climate-CO_2 variations in south-central Texas during the late Quaternary. *Quat. Res.* **58**, 182–188 (2002).

Acknowledgements

We thank C. Bell and E. Lundelius for discussions, and T. Wicks for assistance in fieldwork and data analysis. We thank T. D. Hall and B. Hall of Hall's Ranch for access to the site. T.M.S. received partial support for this work from the National Science Foundation AGS1702271 and from a UT system-CONACYT collaborative research grant (ConTex grant no. 2017-33).

Author contributions

T.M.S., N.P.M. and P.D.R. designed the study. T.M.S. facilitated and conducted the fieldwork. T.M.S. and C.S. conducted the laboratory work and analysed the data. C.S., P.N.D. and N.P.M. analysed the climate model output. T.M.S., C.S. and P.N.D. conducted the data–model analysis. T.M.S. and C.S. wrote the paper. C.S. created the figures. All authors contributed to editing the final version of the manuscript.

Competing interests

The authors declare no competing interests.

Additional information

Extended data is available for this paper at https://doi.org/10.1038/s41561-021-00860-8.

Supplementary information The online version contains supplementary material available at https://doi.org/10.1038/s41561-021-00860-8.

Correspondence and requests for materials should be addressed to Chijun Sun.

Peer review information *Nature Geoscience* thanks Tripti Bhattacharya and the other, anonymous, reviewer(s) for their contribution to the peer review of this work. Primary Handling Editor: James Super.

Reprints and permissions information is available at www.nature.com/reprints.

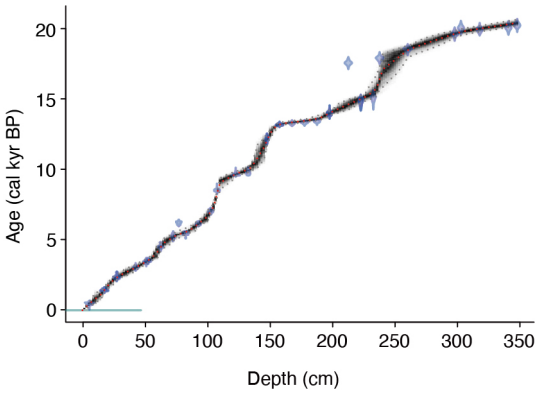

Extended Data Fig. 1 | Age-depth model for Hall's Cave sediment core. Modeled age-depth relationship based on 37 AMS radiocarbon dates made primarily on bone collagen. The age-depth model is made using the Bayesian age-depth modeling program BACON[50]. Purple violin plots show the probability-density function for each calibrated radiocarbon age-estimate. The solid red line indicates the weighted mean of all possible chronologies. The grey-scale shading indicates uncertainties in modeled age depth relationships, and the dotted black lines indicate 95% confidence intervals.

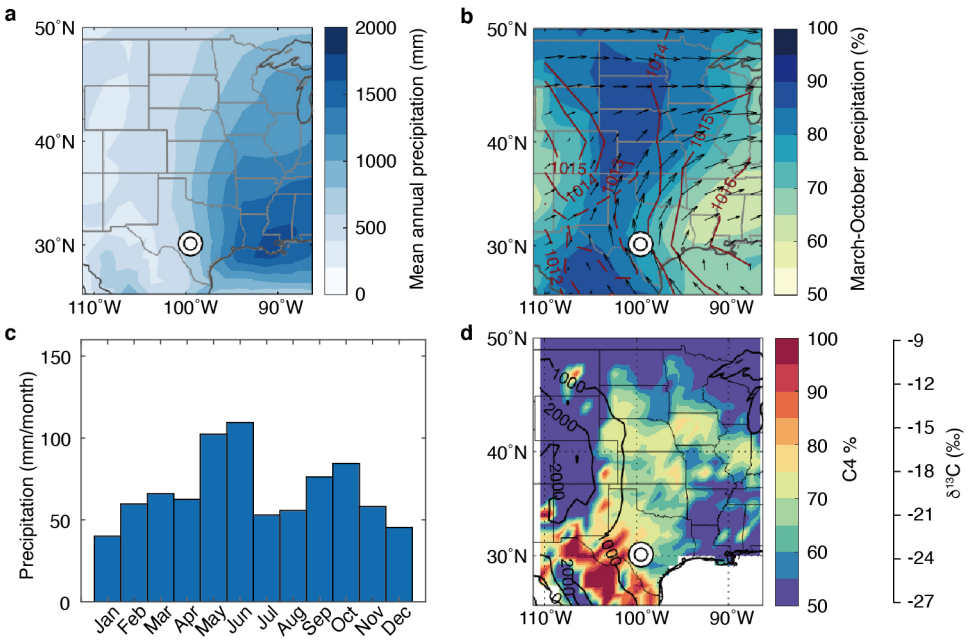

Extended Data Fig. 2 | Modern climatology and vegetation distribution in the southern Great Plains. (**a**) Long-term (1981-2010) mean annual precipitation (MAP; mm/year). The circle indicates the location of Hall's Cave. (**b**) The proportion of warm-season (March – October) precipitation relative to the annual total. Contours indicate March-October sea-level pressure, and vectors indicate March-October 850 hPa wind. (**c**) Monthly mean precipitation at the location of Hall's Cave. Precipitation data is from Global Precipitation Analysis (GPCP). All other climatological data are from NCEP-NCAR Reanalysis 1[59]. (**d**) Distribution of C_4 vegetation across the region. Data from the International Satellite Land-Surface Climatology Project, Initiative II[60]. Secondary axis describes the distribution of $\delta^{13}C$ values of terrestrial vegetation, calculated using a linear mixture model between C_3 and C_4 plants with endmember values of −27‰ and −9‰, respectively. Contours indicate elevation (meter).

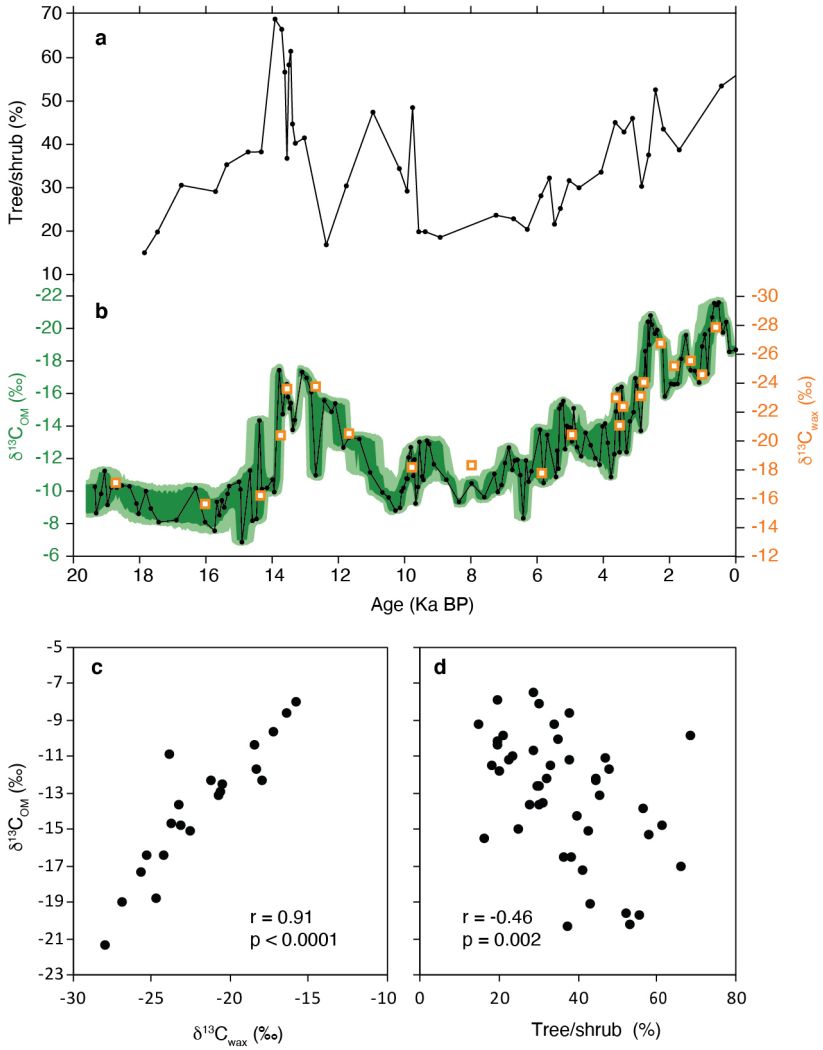

Extended Data Fig. 3 | Comparison between $\delta^{13}C_{OM}$, $\delta^{13}C_{wax}$, and a pollen record from Hall's Cave showing strong correlations between each other. (**a**) The percentage of tree and shrub pollen count[15]. (**b**) $\delta^{13}C_{OM}$ and $\delta^{13}C_{wax}$. (**c**) Scatterplot of $\delta^{13}C_{OM}$ vs. $\delta^{13}C_{wax}$. (**d**) Scatterplot of $\delta^{13}C_{OM}$ vs. percentage of tree/shrub pollens.

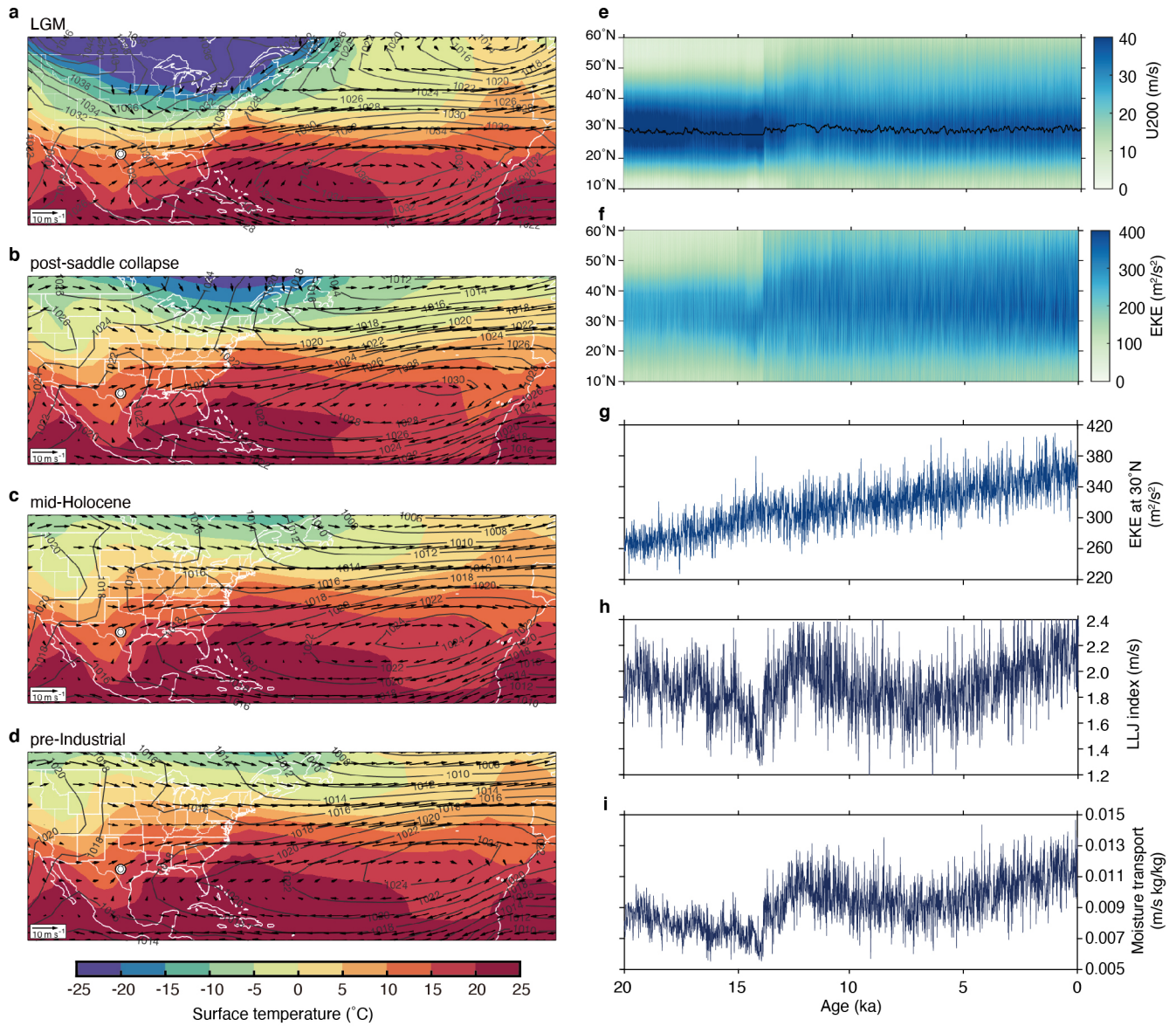

Extended Data Fig. 4 | Evolution of springtime North American climate over the last 20,000 years in TraCE-21ka. (**a-d**) Simulated springtime climatology during (a) the Last Glacial Maximum with the southern Great Plains dominated by westerly wind, (b) post-saddle collapse with a greatly intensified LLJ, (c) mid-Holocene, and (d) pre-Industrial. Color shading indicates surface temperature. Contours indicate sea-level pressure. Vectors indicate 850 hPa wind. (**e**) Springtime 200 hPa zonal wind speed averaged within a longitudinal band (95°–103°W). The black line indicates the latitude of maximum U200 wind speed. (**f**) Springtime 200 hPa eddy kinetic energy (EKE) averaged within a longitudinal band (95°–103°W). (**g**) Springtime 200 hPa EKE over the southern Great Plains at 30°N. (**h**) The springtime Low-Level Jet index. (**i**) Springtime meridional moisture transport by the LLJ, calculated as the mean specific humidity (Q) multiplied by the LLJ index.

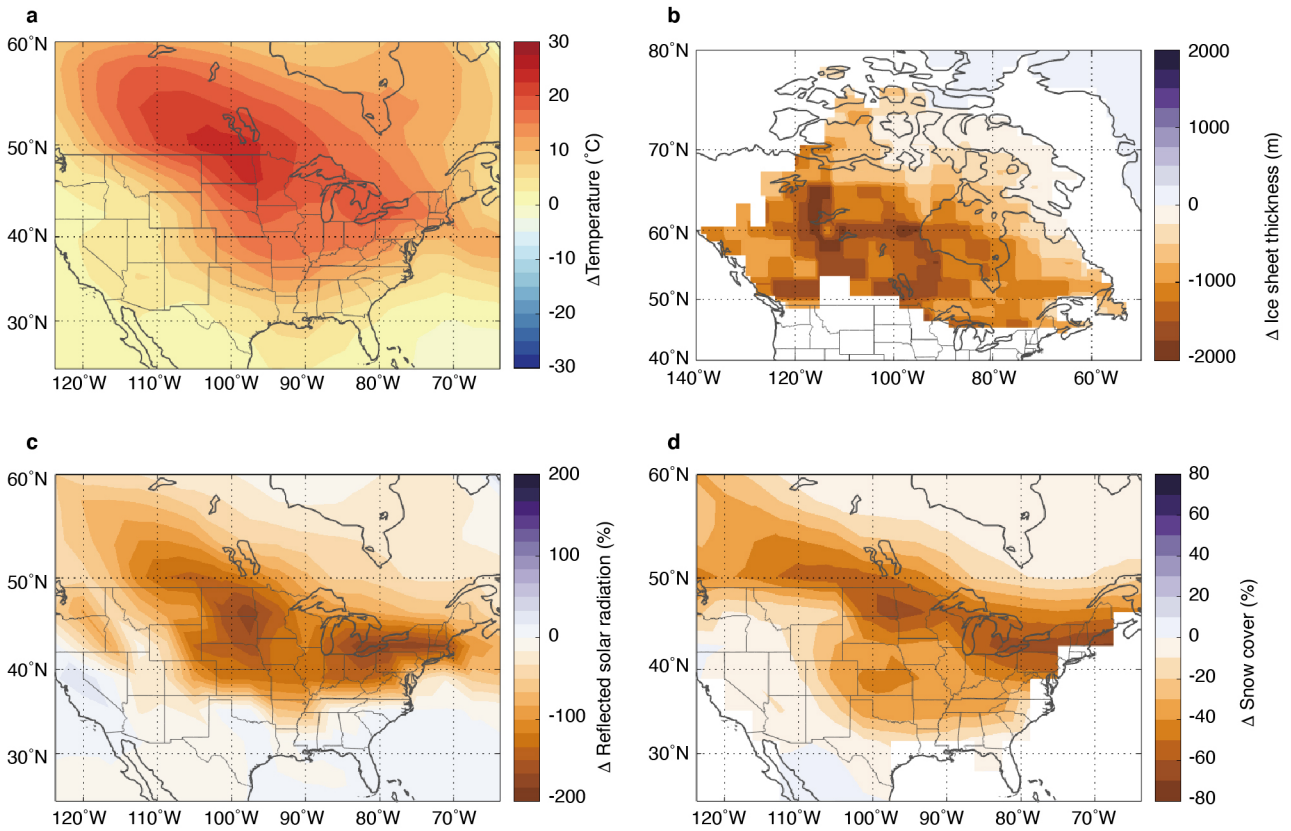

Extended Data Fig. 5 | Changes in land surface conditions over North America induced by the 'saddle collapse' (11-13ka minus LGM). (**a**) Changes in springtime surface temperature. (**b**) Changes in ice sheet thickness. (**c**) Changes in springtime reflected solar radiation (**d**) Changes in snow cover.

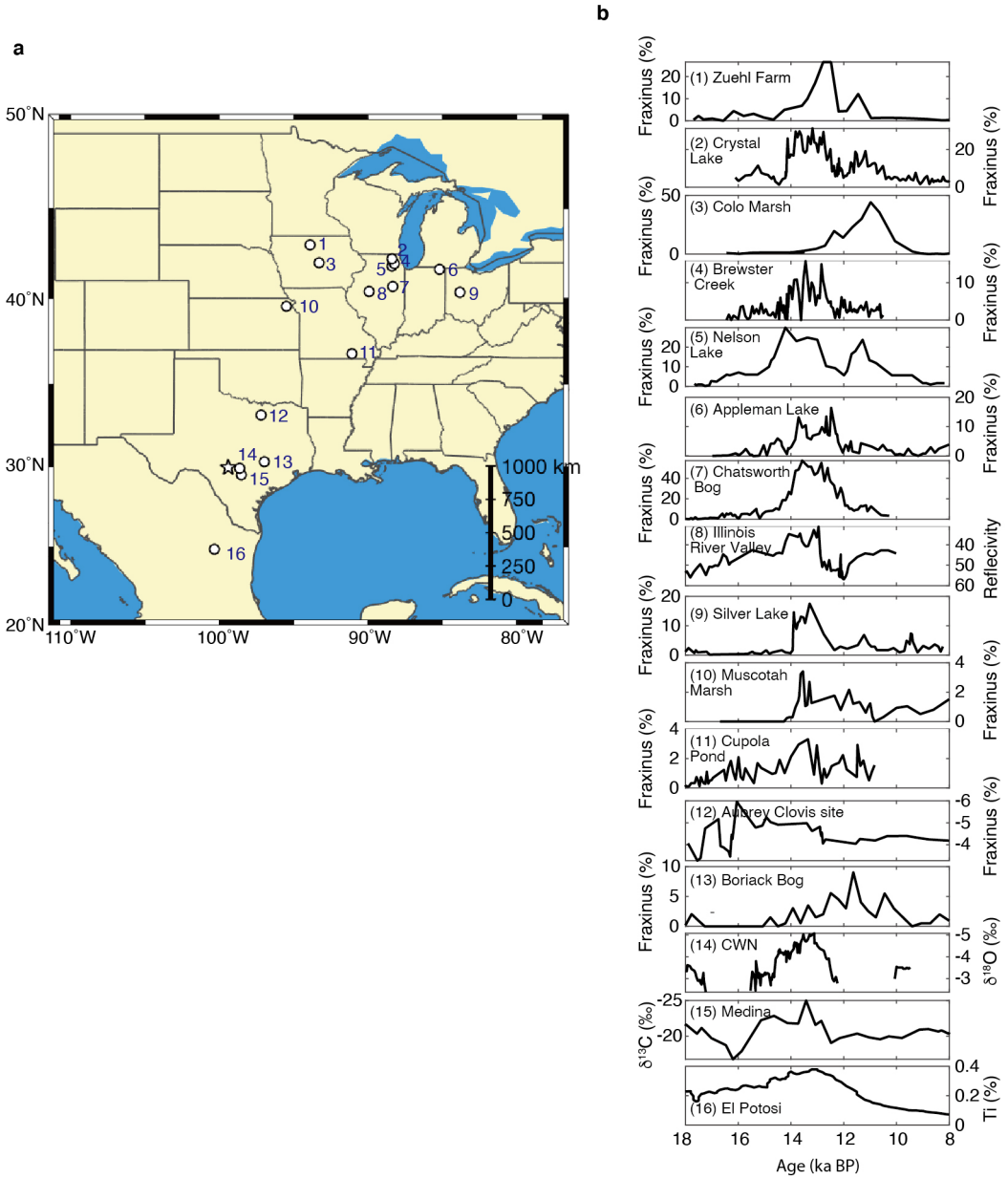

Extended Data Fig. 6 | Synthesis of deglacial hydroclimate records in the central United States and northeastern Mexico showing a regionally consistent change towards wetter conditions. (**a**) Map showing the sites of the records plotted in (b), which are labeled from (1) to (16). Star indicates the location of Hall's Cave. (**b**) Hydroclimate records from the central U.S. showing wetter conditions during the last deglaciation. From north to south: (1) Zuehl Farm site[61]; (2) Crystal Lake[27]; (3) Colo Marsh[61]; (4) Brewster Creek[62]; (5) Nelson Lake[63]; (6) Appleman Lake[28]; (7) Chatsworth Bog[63]; (8) Illinois River Valley[64]; (9) Silver Lake[65]; (10) Muscotah Marsh[66]; (11) Cupola Pond[29]; (12) Aubrey Clovis site[67]; (13) Boriack Bog[68]; (14) Cave without a Name[69]; (15) Medina River[70]; (16) El Potosi[30].

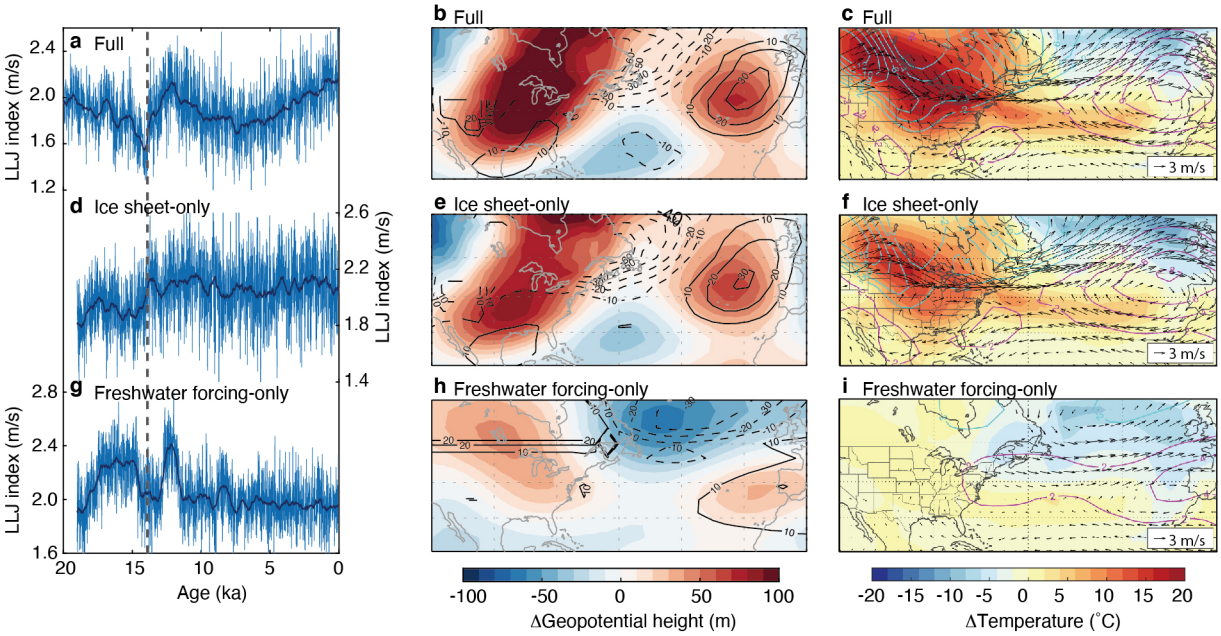

Extended Data Fig. 7 | Comparison of deglacial climate changes simulated in TraCE full, ice sheet-only, and Freshwater forcing-only runs. (**a**) Evolution of the springtime LLJ in the Full simulation. Light blue line is the decadal mean LLJ index calculated from the model output. Dark blue line is 500-yr moving average values of the LLJ index. The dashed line indicates the timing of the ice sheet 'saddle collapse' at 13.9 ka in the TraCE-21ka experiments. (**b**) Changes (11-13ka minus LGM) in the springtime 200 hPa (shadings) and 850 hPa (contours) eddy geopotential height in the TraCE full simulation. (**c**) Changes in the springtime surface temperature (shadings), sea-level pressure (contours), and 850 hPa wind. (**d-f**) Same as (a-c) but for the ice sheet-only single forcing simulation. (**g-i**) Same as (a-c) but for the freshwater forcing-only single forcing simulation.

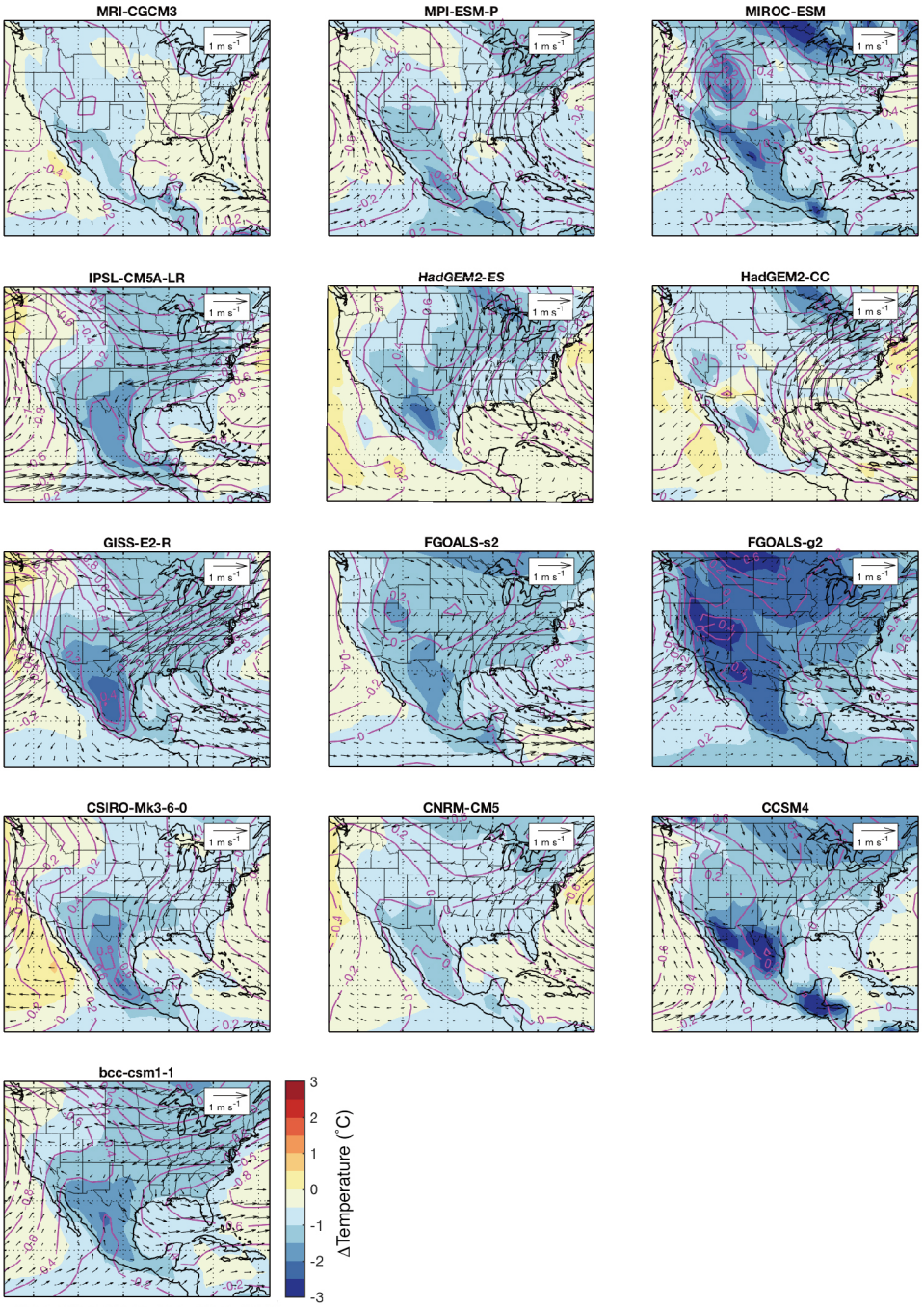

Extended Data Fig. 8 | Mid-Holocene climate change relative to the pre-Industrial in simulations from PMIP3 experiments (6 ka minus 0 ka). Color shading indicates changes in surface temperature (°C). Contours indicate changes in sea-level pressure (hPa). Vectors indicate changes in 850 hPa winds (m/s).